Quantifying the contribution of different cloud types to the radiation budget in southern West Africa

Article

Published Version

Open Access

It is advisable to refer to the publisher's version if you intend to cite from the work. See Guidance on citing.

www.reading.ac.uk/centaur

CentAUR

Central Archive at the University of Reading

Reading's research outputs online

Quantifying the Contribution of Different Cloud Types to the Radiation Budget in Southern West Africa

Peter G. Hill

University of Reading, Reading, United Kingdom

Richard P. Allan

University of Reading, and National Centre for Earth Observation, Reading, United Kingdom

J. Christine Chiu

University of Reading, Reading, United Kingdom, and Colorado State University, Fort Collins, Colorado

Alejandro Bodas-Salcedo

Met Office Hadley Centre, Exeter, United Kingdom

Peter Knippertz

Institute of Meteorology and Climate Research, Karlsruhe Institute of Technology, Karlsruhe, Germany

ABSTRACT

The contribution of cloud to the radiation budget of southern West Africa (SWA) is poorly understood and yet it is important for understanding regional monsoon evolution and for evaluating and improving climate models, which have large biases in this region. Radiative transfer calculations applied to atmospheric profiles obtained from the CERES–CloudSat–CALIPSO–MODIS (CCCM) dataset are used to investigate the effects of 12 different cloud types (defined by their vertical structure) on the regional energy budget of SWA (5°–10°N, 8°W–8°E) during June–September. We show that the large regional mean cloud radiative effect in SWA is due to nonnegligible contributions from many different cloud types; eight cloud types have a cloud fraction larger than 5% and contribute at least 5% of the regional mean shortwave cloud radiative effect at the top of the atmosphere. Low clouds, which are poorly observed by passive satellite measurements, were found to cause net radiative cooling of the atmosphere, which reduces the heating from other cloud types by approximately 10%. The sensitivity of the radiation budget to underestimating low-cloud cover is also investigated. The radiative effect of missing low cloud is found to be up to approximately $-25\,\mathrm{W\,m^{-2}}$ for upwelling shortwave irradiance at the top of the atmosphere and $35\,\mathrm{W\,m^{-2}}$ for downwelling shortwave irradiance at the surface.

1. Introduction

The West African monsoon (WAM) is an important climatological system globally that plays a key role in the climate of sub-Saharan West Africa where many countries rely on the WAM for most of their rainfall (e.g., Nicholson and Grist 2003). Despite its importance, WAM precipitation is not well represented in climate models, which are unable to reproduce the observed intermittence and intraseasonal variability of precipitation in West Africa (Roehrig et al. 2013). Moreover, large differences exist between the accumulated WAM precipitation simulated by different models (Hourdin et al. 2010). These errors lead to a large spread and low confidence in projections of future precipitation in West Africa in climate models (e.g., Cook and Vizy 2006; Paeth et al. 2011).

WAM precipitation is difficult to model because it depends on a number of complex factors, including, but

ⓐ Denotes content that is immediately available upon publication as open access.

Corresponding author: Peter G. Hill, p.g.hill@reading.ac.uk

not limited to, the regional energy budget. Numerous modeling studies have shown the sensitivity of the WAM circulation to changes in the modeled shortwave (SW) and longwave (LW) radiation. Tompkins (2005) and Rodwell and Jung (2008) showed circulation and precipitation differences over West Africa arising from the direct radiative effect of aerosol climatology changes in the European Centre for Medium-Range Weather Forecasts (ECMWF) model. The strength of the WAM in the Met Office Unified Model (UM) is also affected by changes to clouds and hence radiation (Marsham et al. 2013; Birch et al. 2014). More recently, Li et al. (2015) highlighted a strong sensitivity of the WAM circulation and associated precipitation to the radiation schemes used in their simulations.

Given this sensitivity of the WAM circulation and precipitation to radiation budget changes, it is important to ensure that simulated radiative properties in models are realistic. Unfortunately, climate models have large cloud and hence radiation errors in this region (Roehrig et al. 2013). These model errors are persistent in higher-resolution simulations (Stein et al. 2015), and particularly large in southern West Africa (SWA) during the summer (Hannak et al. 2017). Reducing these model errors requires an improved understanding of how clouds affect the radiation budget of West Africa, but the complex cloud climatology with frequent multilayer clouds in this region (Stein et al. 2011) makes it difficult to identify cloud types and to attribute model errors to different cloud regimes. A lack of surface-based cloud observations (e.g., Knippertz et al. 2015b) and uncertain aerosol–cloud interactions (e.g., Knippertz et al. 2015a) further limit understanding of clouds in this region.

The main objective of this article is to quantify the occurrence and radiative effects of different cloud types in the SWA region during the monsoon season. Previous studies have quantified cloud radiative effects for different cloud types on global scales (e.g., Hartmann et al. 1992; Futyan et al. 2005; Oreopoulos et al. 2017). In West Africa, detailed analyses of cloud radiative effects have been limited to a single location (Niamey, Niger) north of SWA (Bouniol et al. 2012; Miller et al. 2012; Collow et al. 2016). Consequently, the radiative effects of different cloud types have yet to be quantified and remain highly uncertain in SWA. Low clouds are prevalent in SWA during the summer (e.g., Schrage et al. 2007; Schuster et al. 2013; van der Linden et al. 2015; Adler et al. 2017) but poorly represented in climate models (Knippertz et al. 2011). Low clouds are also difficult to observe with satellites as they are often obscured by higher clouds (van der Linden et al. 2015; Hill et al. 2016) and as a result remain poorly understood in this region. Consequently, we place a particular emphasis on low clouds in this study. To capitalize on the profiling capability of active remote

sensing, we use the CERES–*CloudSat*–*CALIPSO*–MODIS (CCCM) dataset (Kato et al. 2010, 2011; Ham et al. 2017), which combines observations from active and passive instruments. Using CCCM data as input to radiative transfer calculations, we can investigate radiative effects of different cloud types at the top of the atmosphere (TOA), at the surface, and on heating and cooling in the atmosphere.

2. Methods

a. CCCM dataset and radiative transfer calculations

In this study, we calculate and analyze cloud radiative effects for June–September in the region bounded by 5°–10°N, 8°W–8°E. This time period and region was chosen to coincide with previous and ongoing research within the Dynamics–Aerosol–Chemistry–Cloud Interactions in West Africa (DACCIWA) project (e.g., Knippertz et al. 2015b; Hill et al. 2016; Hannak et al. 2017). Moreover, this domain strikes a balance between being sufficiently large to minimize statistical sampling errors and being sufficiently homogeneous for domain mean values to remain meaningful. We use release B1 of the CCCM dataset (Kato et al. 2010, 2011; Loeb 2008), which is available from July 2006 to April 2011 inclusive. As this study focuses on the monsoon season (defined as June–September) over SWA, the resulting data length is 19 months. The satellites used to generate the CCCM product are polar orbiting, crossing the equator at approximately 0130 and 1330 local time.

The CCCM dataset contains those CERES and MODIS footprints that correspond to the *CloudSat*–*CALIPSO* ground track (Fig. 1). Clouds and the Earth's Radiant Energy System (CERES) and Moderate Resolution Imaging Spectroradiometer (MODIS) are passive instruments providing information on the radiative properties at the TOA, while the *CloudSat* radar and *Cloud–Aerosol Lidar and Infrared Pathfinder Satellite* (*CALIPSO*) lidar are active instruments that provide detailed vertical structure. The CERES optical footprint is 20 km; adding the time response results in a point-spread function of approximately 35 km. Consequently, each CERES footprint contains approximately 30 *CloudSat* profiles and 100 *CALIPSO* profiles.

To reduce data volumes, the *CloudSat*–*CALIPSO* profiles within each footprint are grouped based on their vertical structure. First *CloudSat* and *CALIPSO* observations are merged on to a common 1 km × 1 km horizontal grid. Within each profile, cloud-top and cloud-base height for up to six cloud layers are estimated from the *CloudSat* cloud classification product and the *CALIPSO* vertical feature mask. Profiles with the same
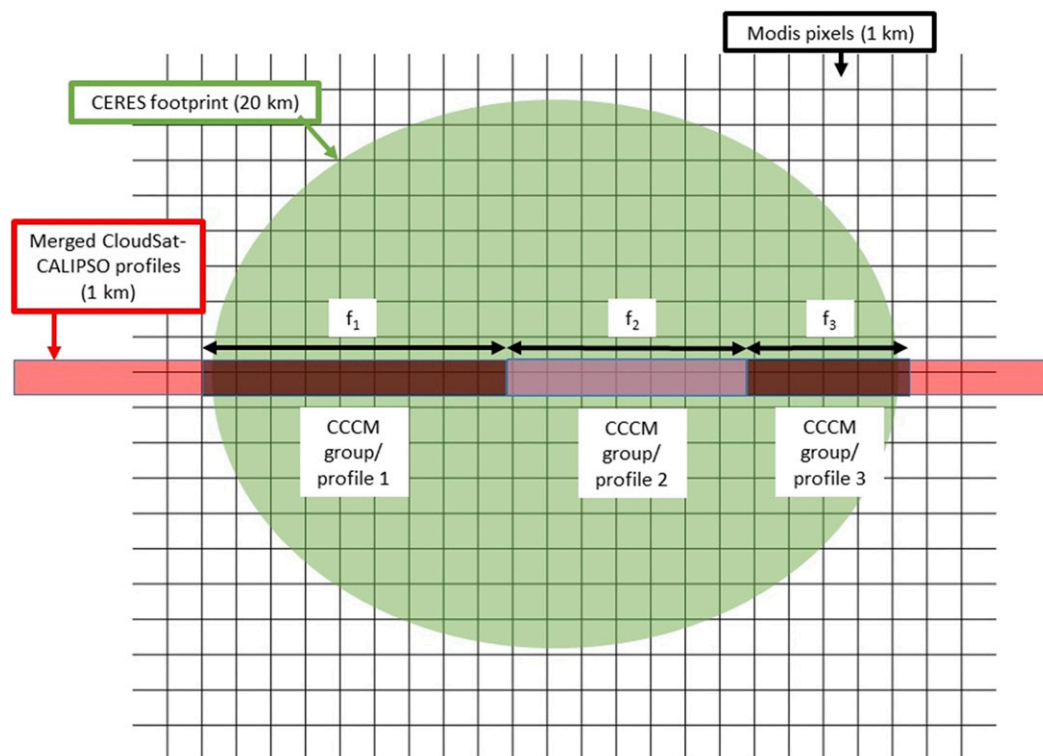
FIG. 1. Schematic illustrating how measurements from different instruments are combined to form CCCM group profiles (also known as cloud groups) in the CCCM dataset. Based on Kato et al. (2011).

cloud-top and cloud-base height are combined to form up to 16 cloud groups. For further details on the grouping process, see Kato et al. (2010). For each cloud group, cloud properties are derived from a combination of *CloudSat*, *CALIPSO*, and MODIS measurements, as described by Bodas-Salcedo et al. (2016), with a vertical resolution of approximately 240 m. For simplicity, we shall refer to these groups as "CCCM group profiles" hereafter.

The CCCM dataset is used as input to radiative transfer calculations using the Suite of Community Radiative Transfer Codes (SOCRATES) two-stream radiation scheme (Edwards and Slingo 1996) to obtain radiative fluxes and heating rates for each profile. The CCCM group profiles provide cloud water content and liquid droplet effective radius. Temperature, water vapor, and surface and aerosol properties are also obtained from the CCCM dataset, as described below, but do not vary within CERES footprints. The CCCM dataset includes calculated profiles of irradiances and heating rates for each CERES footprint; our new calculations are necessary to provide irradiances and heating rates for the individual cloud groups within each CERES footprint, which are not available in the CCCM product.

The treatment of cloud in our radiative transfer calculations follows Bodas-Salcedo et al. (2016), except for two changes. First, we changed the cloud phase when the combination of cloud temperature [based on Goddard Earth Observing System Model (GEOS) reanalyses] and cloud phase (based on the *CloudSat* phase) reported by CCCM was unphysical (i.e., water cloud at temperatures below 233 K and ice cloud at temperatures above 273 K). Our second change relates to the parameterization used within the radiative transfer model to calculate the single scattering properties of clouds from the cloud bulk microphysical properties. We use a different parameterization of ice single scattering properties (Baran et al. 2013) because it results in better agreement between our calculations and the CERES measurements at the TOA. Our radiative transfer calculations were quite sensitive to the choice of parameterization of ice single scattering properties. For example, using a different parameterization of ice single scattering properties (Baran et al. 2016) in our calculations increases the mean TOA cloud radiative effects for all high cloud types, by 27–78 W m^{-2} for SW and by 5–21 W m^{-2} for LW radiation.

The CCCM dataset provides a profile of aerosol type and mean aerosol extinction for each CERES footprint. Seven common aerosol species are represented, including soluble and insoluble particles, small and large dust particles, sulfuric acid, sea salt, and soot. The spectrally varying extinction, single scattering albedo, and
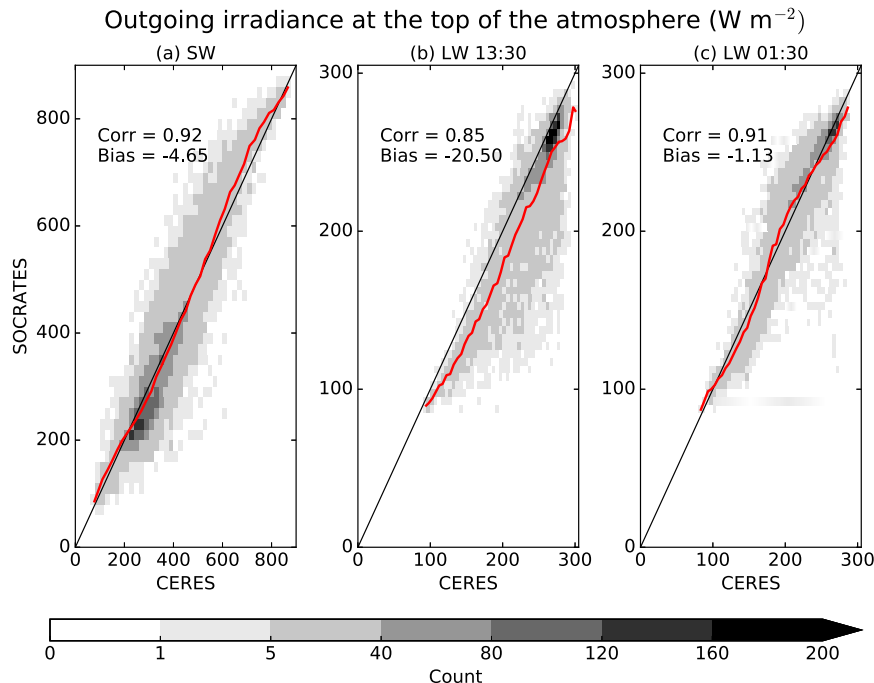
FIG. 2. Comparison of SOCRATES-calculated (a) SW and (b),(c) LW outgoing irradiances at the TOA with collocated CERES observations that are taken from the integrated CCCM product. SOCRATES values are weighted means of the calculations for each CCCM cloud group within the corresponding CERES footprint, where the weighting is determined by the fraction of the CERES footprint occupied by each cloud group. Shading represents joint frequency of occurrence. Correlation coefficient and bias (W m^{-2}) with respect to CERES observations are listed in each panel.

asymmetry of these aerosol species are parameterized in SOCRATES as a function of aerosol mass mixing ratio, as described in Cusack et al. (1998). For each aerosol type, we use the inverse of the SOCRATES parameterization of extinction to derive profiles of aerosol mass mixing ratios from the aerosol extinction profiles. These aerosol mass mixing profiles are used as input to the SOCRATES calculations, ensuring that the aerosol extinction profiles in our calculations and the CCCM dataset match.

Our radiative transfer calculations require knowledge of surface albedo in the SW spectral region and surface emissivity in the LW region. When available, we take MODIS narrowband surface albedo measurements from the CCCM product, which are converted to average albedo values for the SOCRATES spectral bands through linear interpolation with weighting by the solar spectrum. When the MODIS surface spectral albedo is not available, the broadband surface albedo from CERES is applied over land, and a broadband surface albedo as a function of solar zenith angle (Taylor et al. 1996) is applied over ocean. In the LW spectral region, the surface emissivity from CERES products is applied for all cases.

b. Validation of calculations

To evaluate the reliability of these calculations, we perform a point-to-point comparison between calculated irradiances at the TOA and coincident CERES observations, as shown in Fig. 2. SOCRATES irradiances corresponding to different CCCM groups are weighted by the fraction of the corresponding CERES footprint they occupy. Because of differences in swath and pixel sizes between the different instruments (e.g., Fig. 1), the CCCM group profiles used for our radiative transfer calculations correspond to a narrow swath within the coincident CERES footprint, rather than the entire footprint. This representativeness difference may lead to nonnegligible discrepancies between calculated and CERES-observed irradiances. However, we expect these discrepancies to be random rather than systematic; therefore, this intercomparison provides a fair evaluation of our calculations. In general, the calculations show good agreement with the CERES measurements. The calculated outgoing SW radiation (OSR) flux has a bias of -4.65 W m^{-2} and a Pearson correlation coefficient of 0.92 with the CERES observations. For the outgoing LW radiation (OLR) fluxes there are notable

day–night differences: at night the bias is $-1.13\,\mathrm{W\,m^{-2}}$ and the correlation is 0.91, whereas during the day the bias is larger ($-20.50\,\mathrm{W\,m^{-2}}$) and the correlation is smaller (0.85). The large daytime bias in OLR flux is evident in Fig. 2b, as a significant proportion of the calculated irradiances are much lower than the coincident CERES observations.

The potential causes of the large bias in the calculated daytime OLR flux include the input CCCM group profiles and the approximations made in the SOCRATES scheme. The representativeness difference, highlighted above, is not expected to cause systematic differences between the calculations and the CERES observations. For each CERES footprint, the CCCM dataset includes radiative fluxes computed using various different treatments of clouds and aerosol. Interestingly, the CCCM irradiance calculations suffer from a similar magnitude daytime OLR bias in the DACCIWA region (Ham et al. 2017). The large bias also persists when we reran SOCRATES with the temperature-dependent parameterization of ice optical properties described by Baran et al. (2016). These findings help rule out the possibility that the OLR bias is due to the radiative transfer models themselves.

Cloud extinction within each CCCM group profile is normalized so that the total cloud optical depth matches that retrieved from MODIS. As different algorithms are used to retrieve cloud optical depth from MODIS measurements during the day and at night (Minnis et al. 2011), differing biases between day and night may be expected. However, one would expect the MODIS optical depth retrieval to be more reliable during the day when the SW radiation measurements provide additional information. The OSR bias is relatively small, which suggests that the daytime total cloud optical depth is reasonable. Consequently, the error in the CCCM group profiles is most likely in the vertical distribution of cloud extinction, which has a large effect on the OLR but little effect on OSR.

One possible bias in the input CCCM group profile is the misattribution of low-cloud extinction detected by MODIS to higher-altitude cloud in the CCCM dataset, because of undetected low-cloud layers. The combined active measurements from *CALIPSO* and *CloudSat* provide the best satellite-based estimate of low cloud, but detection of low cloud remains challenging in some scenarios. For example, *CloudSat* is unable to detect all boundary layer clouds as a result of ground clutter, and *CALIPSO* is unable to detect lower clouds when high clouds with optical depth greater than 2–3 exist and completely attenuate the lidar signal (Mace et al. 2009). Low cloud is more common during the day as

discussed in section 3, so this problem is likely to be more significant during the day. If low cloud is missing in the *CloudSat* and *CALIPSO* profiles, then the normalization of optical depth by MODIS may lead to an attribution of low-cloud extinction to higher-level clouds. This would lead to a reduction in OLR, while having little impact on the OSR, which is consistent with the daytime SOCRATES calculations. We shall refer to this as the "low-cloud misattribution" hypothesis throughout this article.

c. Diurnal mean approximation

Surface-based synoptic and geostationary satellite observations show maximum low cloud occurrence in SWA at approximately 1000 UTC and minimum at 1800 UTC (van der Linden et al. 2015). Moreover, like much of the tropics, SWA has a diurnal cycle in high cloud linked to the occurrence of convection, with more high cloud at night than during the day (e.g., Hill et al. 2016). As the CCCM product is based on polar-orbiting satellite measurements, it overpasses SWA at only two points in the diurnal cycle and clearly will not capture this complex cloud diurnal variability. However, estimates of the diurnal mean irradiances are required to analyze the contribution of different cloud types to the mean radiation budget.

We use different methods to approximate the diurnal mean radiative effect of different cloud types in the SW and LW regions. For a SW diurnal mean approximation, we conducted further calculations with solar zenith angles corresponding to each hour of the diurnal cycle. The hourly calculations based on 1330 LT profiles were averaged together to approximate the diurnal mean, as we assume 1330 LT cloud properties are more representative of mean daylight conditions than 0130 LT cloud properties. The hourly calculations based on 0130 LT profiles are averaged together to obtain a second estimate, which we use to derive the uncertainty resulting from diurnal changes in cloud, as described in section 2e. For the LW diurnal mean approximation, we simply average the mean irradiances at 1330 and 0130 LT, which is consistent with several previous studies (e.g., Hong et al. 2016).

To evaluate our diurnal mean approximations, we compare our results to Geostationary Earth Radiation Budget (GERB) measurements of TOA irradiances (Harries et al. 2005; Dewitte et al. 2008) for the same time period and region as CCCM. With a temporal resolution of 15 min the GERB high-resolution (HR) measurements resolve the diurnal cycle of TOA irradiances. The GERB product does not report OSR fluxes for solar zenith angles larger than 80°. For zenith angles between 86.5° and
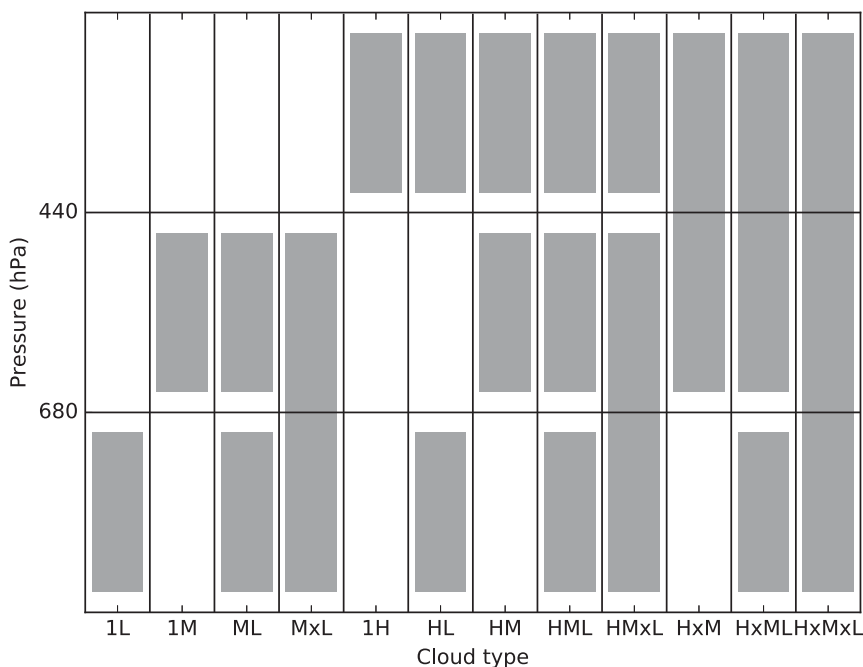
FIG. 3. Illustrative schematic of the 12 cloud types used in this study. Low-, mid-, and high-level clouds are separated using pressure levels of 680 and 440 hPa. The letter x between two layers indicates they are contiguous in the vertical extent.

104.5°, we use mean twilight values from CERES (Kato 2003). For zenith angles between 80.0° and 86.5°, where CERES twilight values are not reported, we use linear interpolation in time between the GERB measurements and the CERES twilight values.

For OSR, GERB has a regional diurnal mean of $149 \, \mathrm{W \, m^{-2}}$. Applying our SW diurnal mean approximation to our SOCRATES calculations results in a regional mean OSR of $144 \, \mathrm{W \, m^{-2}}$ when we use the 1330 LT CCCM data, and $125 \, \mathrm{W \, m^{-2}}$ when we use the 0130 LT CCCM data. Estimating the OSR using the LW diurnal mean approximation [i.e., by averaging the mean OSR at 1330 LT ($376 \, \mathrm{W \, m^{-2}}$) and the mean OSR at 0130 LT ($0 \, \mathrm{W \, m^{-2}}$)] gives an OSR of $188 \, \mathrm{W \, m^{-2}}$. For OLR, GERB has a regional mean of $230 \, \mathrm{W \, m^{-2}}$. Applying our LW diurnal mean approximation to our SOCRATES calculations results in a regional mean of $220 \, \mathrm{W \, m^{-2}}$. We can separate the calculation bias and the LW diurnal mean approximation bias by applying our LW diurnal mean approximation to the CERES OLR measurements in the CCCM product, as these measurements represent the OLR we would obtain if the calculations were unbiased. Applying the LW diurnal mean approximation to the CERES measurements results in the same value as averaging the GERB diurnal mean: $230 \, \mathrm{W \, m^{-2}}$. This shows that the bias in the LW diurnal mean approximation when applied to our

LW calculations is due to the bias in the calculated OLR at 1330 LT.

d. Definition of cloud types and cloud radiative effects

Based on the classification scheme described in Tselioudis et al. (2013), we assign a cloud type to each CCCM group profile, based on cloud vertical structure. Pressure thresholds of 680 and 440 hPa are used to classify each CCCM group profile according to whether it contains one or more of low- (L), mid- (M), or high-level (H) cloud and whether cloud in different layers is connected or not. As illustrated in Fig. 3, this classification results in 13 different cloud scene types: clear sky and 12 cloud types. Cloud occurring in multiple layers is denoted by a letter for each layer it occurs in, while the letter x is used to denote when cloud extends across the pressure boundaries. For convenience, we use "isolated low cloud" to refer to CCCM group profiles that contain only low cloud (i.e., 1L), "discontiguous low cloud" to refer to low cloud that occurs beneath distinct higher clouds (i.e., ML, HL, HxML, and HML), and "contiguous low cloud" to refer to scenes where the cloud extends vertically from the low layer to higher layers (i.e., MxL, HMxL, and HxMxL). Note that passive sensors can only identify isolated low clouds, since high clouds in the other two categories will obscure low clouds.

In this article we calculate the cloud radiative effect (CRE) by

$$\text{CRE} = (I_\downarrow^{\text{all}} - I_\uparrow^{\text{all}}) - (I_\downarrow^{\text{clr}} - I_\uparrow^{\text{clr}}), \tag{1}$$

where I^{all} denotes the all-sky irradiance calculated by SOCRATES, I^{clr} is the clear-sky irradiance, calculated by repeating the SOCRATES calculations without cloud, $I_\downarrow$ denotes a downwelling irradiance, and $I_\uparrow$ denotes an upwelling irradiance. This method is applied to calculate both TOA and surface CREs; in-atmosphere CREs are calculated by subtracting the surface CRE from the TOA CRE.

Let $f_{i,j}$ be the fraction of the ith CERES footprint occupied by the jth CCCM group profile, and $\text{CRE}_{i,j}$ be the corresponding CRE (Fig. 3). Then the regional mean CRE can be calculated by

$$\text{CRE} = \frac{\sum_i \left(\sum_{j=1}^{n_i} f_{i,j} \text{CRE}_{i,j} \right)}{\sum_i \left(\sum_{j=1}^{n_i} f_{i,j} \right)}, \tag{2}$$

where n_i is the number of CCCM group profiles (at most 16) in the ith CERES footprint.

After classification, each CCCM group profile corresponds to one of 13 cloud scene types. The contribution from each scene type to the regional mean CRE (CRE^k) can be calculated by

$$\text{CRE}^k = \frac{\sum_i \left(\sum_{j=1}^{n_i} \delta_{t(i,j)k} f_{i,j} \text{CRE}_{i,j} \right)}{\sum_i \left(\sum_{j=1}^{n_i} f_{i,j} \right)}, \tag{3}$$

where $t(i, j)$ is the cloud scene type of the jth CCCM group profile in the ith CERES footprint and $\delta_{t(i, j)k}$ is the Kronecker delta function, which equals one if $t(i, j) = k$ and zero otherwise. This $\delta_{t(i, j)k}$ term ensures that only cloud scenes of type k are included in the contribution of scene type k to the regional mean CRE.

Using these 13 cloud scene types, since each CCCM group profile is assigned to a single scene type, we can rewrite the CRE as

$$\text{CRE} = \sum_{k=1}^{13} \text{CRE}^k. \tag{4}$$

Since the CRE for the clear-sky scene is zero, in practice we only need to sum over the 12 cloud types.

To provide further insight into how different cloud types affect the regional energy budget, the contribution to the total cloud radiative effect from each cloud type CRE^k [Eq. (3)] can be further decomposed into its frequency of occurrence F^k and mean coincident cloud radiative effect CCRE^k (the mean radiative effect calculated using only the CCCM group profiles that correspond to that cloud type). The term F^k is calculated by summing the fraction of each CERES footprint assigned to that cloud type k and dividing by the total number of CERES footprints:

$$F^k = \frac{\sum_i \left(\sum_{j=1}^{n_i} \delta_{t(i,j)k} f_{i,j} \right)}{\sum_i \left(\sum_{j=1}^{n_i} f_{i,j} \right)}. \tag{5}$$

CCRE^k is calculated by averaging the CREs for all the CCCM group profiles assigned to cloud type k, weighted by the fraction of a CERES footprint assigned to each CCCM group profile:

$$\text{CCRE}^k = \frac{\sum_i \left(\sum_{j=1}^{n_i} \delta_{t(i,j)k} f_{i,j} \text{CRE}_{i,j} \right)}{\sum_i \left(\sum_{j=1}^{n_i} \delta_{t(i,j)k} f_{i,j} \right)}. \tag{6}$$

Then the contribution from each cloud type to the CRE^k can be calculated by

$$\text{CRE}^k = F^k \text{CCRE}^k. \tag{7}$$

This decomposition can also reveal hidden biases in atmospheric models, where compensating errors in cloud frequency of occurrence and cloud radiative properties can lead to reasonable regional mean irradiances (e.g., Nam et al. 2012).

e. Treatment of uncertainty in cloud radiative effects

We account for three distinct sources of uncertainty in the CREs calculated in this article: sampling, the diurnal approximations, and the radiative transfer calculations. We estimate the uncertainty from each of these sources independently and then derive the total uncertainty by combining them in quadrature.

We perform radiative transfer calculations for a large number of CERES footprints (approximately 9600 daytime and 9100 nighttime footprints). However, as we are not continuously sampling the entire domain, any quantity we derive from these calculations will be subject to a statistical sampling error. We estimate sampling errors by bootstrap sampling of the CERES footprints. The bootstrapping is performed separately for day and

night, and 200 bootstrap samples are used. Uncertainty for each cloud type is then calculated as the standard deviation of the mean CRE^k in each of the bootstrap samples. The magnitude of this uncertainty is quite small; for each of the contributions of the different cloud types to the regional mean CRE, it is less than $1.5\,W\,m^{-2}$ for both SW and LW radiation.

Given that they are based on only two points in the diurnal cycle, our approximations for the diurnal mean irradiance represent an additional source of uncertainty. The SW diurnal approximation uncertainty is estimated by the absolute value of the difference between the SW diurnal mean approximation (i.e., based on calculations using the 1330 LT CCCM data) and the SW diurnal mean calculations using the 0130 LT CCCM data. For LW radiation, the diurnal approximation uncertainty is estimated by the difference between the LW diurnal mean approximation and the LW radiation calculations at either 1330 or 0130 LT (since the LW diurnal mean is approximated by the average of the 1330 and 0130 LT LW radiation calculations, it does not matter which time we use). The magnitude of the diurnal approximation uncertainty is very variable for different cloud types. The SW diurnal approximation uncertainty is smallest (less than $0.25\,W\,m^{-2}$) for the contribution of HxMxL to the regional mean CRE. The SW diurnal approximation uncertainty is largest (almost $7\,W\,m^{-2}$) for the contribution of 1L to the regional mean CRE. The SW diurnal approximation uncertainty for 1L is large because of large changes in its frequency at 0130 LT compared to 1330 LT (cf. Fig. 4). The diurnal mean approximation uncertainty in the LW radiation is smaller; the largest LW uncertainty is approximately $2.5\,W\,m^{-2}$ for the contribution of HL to the TOA CRE.

To account for uncertainty related to our radiative transfer calculations, we produce a second estimate of the CRE, where we use the comparison with CERES described in section 2b to exclude CCCM group profiles corresponding to large TOA irradiance errors, as explained below. This is referred to as "the constrained dataset" hereinafter. Using the constrained dataset, a second estimate of the coincident cloud radiative effect (CCRE) is calculated for each cloud type. The difference between the CCRE from the full dataset and the constrained dataset is used as an estimate of uncertainty. However, we have no direct evidence that the cloud type frequencies are incorrect (or a justifiable alternative estimate of the cloud type frequencies), so we do not use the constrained dataset to calculate the frequency of occurrence of the cloud types. Thus CRE^k for each cloud type k from the constrained dataset is calculated as the product of the $CCRE^k$ from the constrained dataset and F^k from the full dataset.

To exclude CCCM group profiles with large errors, we need to determine error thresholds for both the SW and LW radiation calculations. Moreover, we do not want to exclude CCCM group profiles where the difference between the calculated irradiance and CERES measurements may be due to the representativeness differences between CERES and *CloudSat–CALIPSO*. As a result, we determine these thresholds based on the mean spatial variability between CERES measurements. We first calculate mean absolute differences in the irradiance for adjacent CERES pixels along the *CloudSat–CALIPSO* flight track. The thresholds are set as the 90th percentile of these differences, with independent thresholds for the SW and LW radiation.

The resulting error thresholds in SW and LW radiation are 132.6 and $28.3\,W\,m^{-2}$, respectively. The difference between our calculations and the corresponding CERES measurements exceeds one of these thresholds for approximately 32.4% of CERES footprints during the day and 21.6% at night. Unsurprisingly, once we exclude these points, the remaining points have improved correlations with CERES observations increasing from 0.92 to 0.95 for the OSR, from 0.85 to 0.97 for the daytime OLR, and from 0.91 to 0.97 for the nighttime OLR. The OLR biases are reduced both for day and night from -20.5 to $-8.9\,W\,m^{-2}$ and from -1.1 to $-0.2\,W\,m^{-2}$, respectively. However, the magnitude of the OSR bias increases from -4.7 to $-12.4\,W\,m^{-2}$. The majority (approximately 56%) of the daytime points that are excluded from this refined dataset are 1H and HL cloud types. This is consistent with the low-cloud misattribution hypothesis, because these are the cloud types for which the extinction from any missing low cloud will be attributed to high cloud and thus have a particularly large effect on the OLR. Generally, the magnitude of the calculation uncertainty is quite small (less than $1.5\,W\,m^{-2}$), with the exceptions being the calculation uncertainty for the contribution of 1H ($\sim2\,W\,m^{-2}$) and HL ($\sim6\,W\,m^{-2}$) to the 1330 LT LW TOA CRE.

As highlighted previously, these three sources of uncertainty are calculated independently and combined in quadrature. For the instantaneous irradiances, we only have sampling and calculation uncertainty and the calculation uncertainty is generally the larger of the two. For diurnal mean irradiances, the SW uncertainty resulting from sampling and the calculations is much smaller than the instantaneous uncertainty at 1330 LT because the diurnal mean SW irradiances are much smaller than the 1330 LT values. For both SW and LW diurnal mean irradiances, the dominant source of uncertainty depends on the cloud type. The largest combined (SW + LW) uncertainty is for 1L as a result of SW
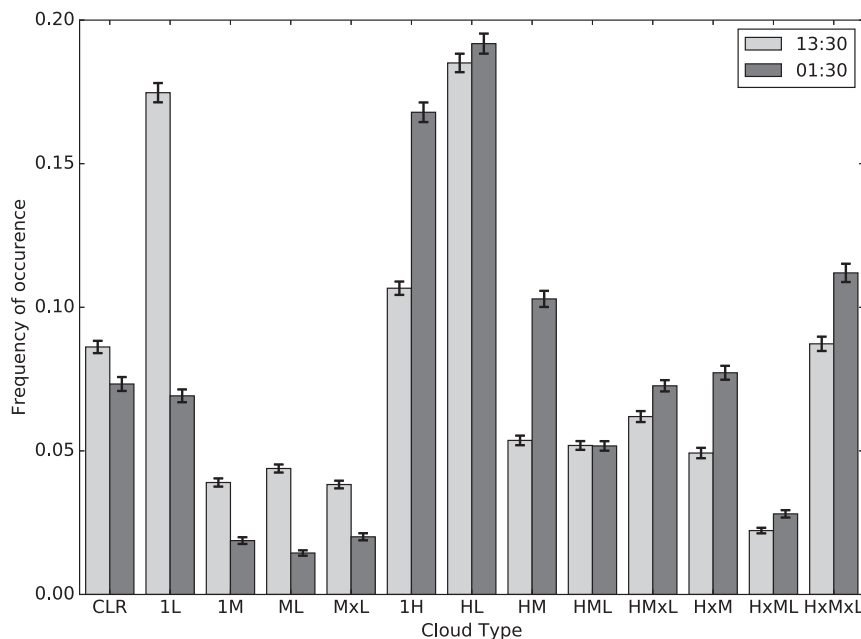
FIG. 4. June–September 2006–10 mean frequency of occurrence of each cloud type in the CCCM product over SWA. Cloud frequency of occurrence at 1330 and 0130 LT are normalized separately. Uncertainty resulting from sampling is illustrated by the error bars, which show the 95% confidence interval based on bootstrapping.

diurnal approximation uncertainty and for HL as a result of calculation uncertainty in the LW radiation.

3. The radiative effects of different cloud types

The frequency of occurrence of the different cloud types is shown in Fig. 4. Cloud frequency of occurrence at 1330 and 0130 LT are calculated and shown separately. SWA is very cloudy, and has infrequent clear sky (less than 10%), in agreement with existing cloud climatologies (e.g., Hill et al. 2016). The most common cloud types are 1L, 1H, and HL, but 8 of the 12 cloud types occur at least 5% of the time in this region, indicating a much more diverse set of cloud types than those found in many other parts of the globe (e.g., Tselioudis et al. 2013; Bodas-Salcedo et al. 2016). Multilayer clouds (i.e., where distinct clouds occur simultaneously in multiple layers) occur frequently (42% during the day and 46% during the night), representing a further source of complexity for understanding cloud radiative effects.

Isolated low cloud (1L) is one of the most common cloud types with a daytime frequency of 17% and a nighttime frequency of 7%. Low cloud occurs even more frequently beneath other cloud layers; the combined isolated and discontiguous low-cloud frequencies are 48% and 36% for daytime and nighttime, respectively. Including contiguous low cloud increases frequencies to 67% during the day and 56% at night, consistent with

the value of 60% reported in Knippertz et al. (2011) based on surface observations at Kumasi, Ghana. The CCCM product may also miss some low cloud beneath high cloud, as explained in the previous section.

The increase in high cloud at night is in agreement with previous analyses of cloud cover in this region from both *CloudSat–CALIPSO* and MODIS (e.g., Stein et al. 2011; Hill et al. 2016), as is the increase in low-cloud cover during the day. However, the Kumasi observations in Knippertz et al. (2011) show similar low-cloud cover at 0130 and 1330 local time. The domain mean increase in low-cloud cover in the CCCM dataset during the day is driven by a larger daytime increase in low-cloud cover to the north of the domain as previously detailed by van der Linden et al. (2015). Including only CCCM data between 6° and 7°N (Kumasi is at 6.7°N), gives smaller day–night differences with total discontiguous low-cloud cover of 50% during the day, and 47% at night.

Figure 5a shows that the mean SW TOA CCRE of each cloud type is strongly linked to the number of layers it extends through, which is an indication of the cloud physical thickness. Physical thickness is in turn correlated with water path and optical depth (Wang et al. 2000). The HxMxL cloud type, which extends into three layers and is likely to be deep convection, has the largest mean SW CCRE (476 W m^{-2} at 1330 LT). Those cloud types that extend between two layers have the next largest mean SW CCRE with values ranging from
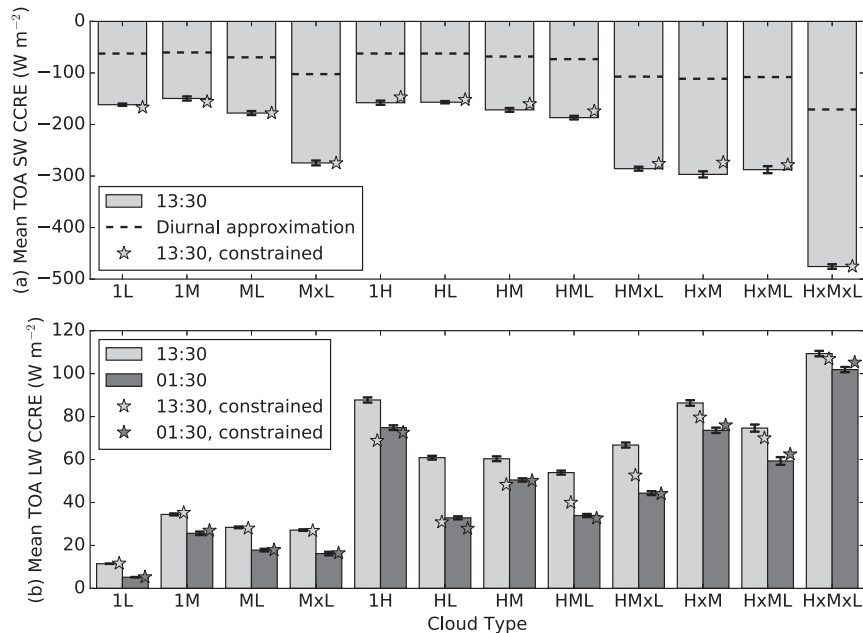
FIG. 5. June–September 2006–10 SOCRATES calculated mean (a) SW and (b) LW mean CCRE at the TOA over SWA. Bars labeled 0130 and 1330 LT correspond to calculations based on the nighttime and daytime satellite overpasses, respectively. The diurnal approximation shown in (a) is based on averaging calculations that use the daytime CCCM data and a range of solar zenith angles, as explained in section 2c. Uncertainty resulting from errors in our calculations is illustrated by the constrained calculations, which exclude CCCM group profiles where the SOCRATES–CERES TOA differences are large, as explained in section 2e. Error bars show the 95% confidence interval based on bootstrapping.

275 to 297 W m^{-2} at 1330 LT. Clouds that occur separately in one or more layers have 1330 LT values ranging from 150 to 187 W m^{-2}.

The diurnal mean downwelling SW irradiance at TOA is approximately 36% of the mean value for the 1330 LT overpasses (not shown). However, for upwelling SW radiation at the TOA, the SW diurnal approximation (indicated by the dashed lines on the bars in Fig. 5a) gives CCRE values between 36% and 40% as large as the instantaneous 1330 LT calculations, depending on cloud type. These ratios differ between cloud types because of the increased atmospheric path length as the solar zenith angle increases. This leads to an increase in the extinction of the direct solar beam resulting from cloud, which has a bigger impact on the SW CCRE of clouds that are less optically thick. Consequently, for the diurnal mean, the relative difference between CCREs for different cloud types is less than for the 1330 LT calculations.

The TOA LW CCRE, shown in Fig. 5b, is of a smaller magnitude than the diurnal mean TOA SW CCRE for almost all cloud types, with isolated high cloud being the exception. As expected the magnitude of LW TOA CCRE is determined by cloud-top temperature, and thus closely linked to the presence of high cloud.

For all cloud types, the LW TOA CCRE is larger during the day than at night. Since TOA downwelling LW irradiances are zero, the LW TOA CCRE is calculated by subtracting the all-sky OLR from the clear-sky OLR. As a result, the LW TOA CCRE can be increased by either increasing the clear-sky OLR or decreasing the all-sky OLR. In the SOCRATES calculations, both these effects occur. A warmer surface temperature during the day leads to a larger value for the clear-sky OLR. Larger ice mass mixing ratios during the day lead to smaller values for the all-sky OLR. The daytime increase in the LW TOA CCRE for isolated low clouds is driven by the increase in the clear-sky OLR. The daytime increase in the LW TOA CCRE for high clouds is driven by larger daytime ice mass mixing ratios. Note that the daytime all-sky OLR is underestimated compared to CERES (Fig. 2b). Moreover, these larger daytime ice mass mixing ratios may not be realistic, and are consistent with the low-cloud misattribution hypothesis.

Using the constrained dataset (i.e., excluding CCCM group profiles where there is a large discrepancy between the calculated and observed irradiances in either the SW or LW), Fig. 5 shows that the exclusion has a
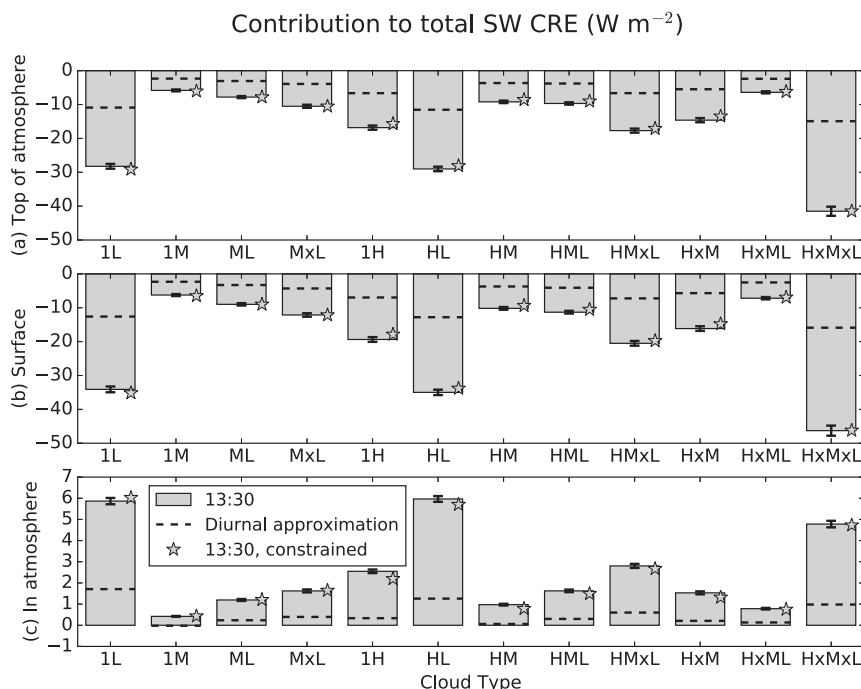
FIG. 6. Contribution to the regional mean SW CRE from each cloud type for June–September, 2006–10 over SWA at (a) TOA, (b) surface, and (c) in the atmosphere, based on SOCRATES calculations. The 1330 LT calculations use the 1330 LT CCCM data with the corresponding solar zenith angle. The SW diurnal approximation is based on averaging calculations that use the 1330 LT CCCM data and a range of solar zenith angles, as explained in section 2c. Uncertainty resulting from errors in our calculations is illustrated by the constrained calculations, which exclude CCCM group profiles where the SOCRATES–CERES TOA differences are large, as explained in section 2e. Error bars show the 95% confidence interval based on bootstrapping.

relatively small effect on the mean daytime SW or nighttime LW CCRE, but has a larger effect on the mean LW daytime CCRE. The biggest effect is for the HL cloud type, where the mean CCRE reduces in magnitude from 61 to 31 W m^{-2}. The H, HM, HML, and HMxL cloud types also have a reduction in magnitude of the mean daytime LW CCRE of 10–20 W m^{-2}. Errors in these cloud types suggest that high clouds are too optically thick, which is consistent with the low-cloud misattribution hypothesis. Intriguingly, the day–night differences in the mean LW CCRE at TOA are reduced, compared to the full dataset. This provides further evidence that the diurnal differences found in the mean TOA LW CCRE in the full dataset may be artificial, because of errors in cloud properties.

Figure 6 shows the contribution to the regional mean SW CRE at TOA, at the surface, and within the atmosphere from each cloud type. The regional mean CRE is simply the sum of the CRE values for each cloud type. At the TOA, three cloud types stand out: vertically deep cloud (HxMxL), high cloud above low cloud (HL), and isolated low cloud (1L). HxMxL has the largest SW CRE

resulting from its large mean CCRE as shown in Fig. 5a. In contrast, 1L and HL have large SW CRE resulting from their relatively high frequency of occurrence as shown in Fig. 4. However, we emphasize that these three cloud types together account for only approximately 50% of the regional mean SW CRE at the TOA; the other cloud types have nonnegligible radiative effects. Indeed, explaining 75% of the regional mean SW CRE requires 6 cloud types, and explaining 90% requires 9 of the 12 cloud types.

The contribution of the 12 different cloud types to the surface CRE (Fig. 6b) is similar to the TOA both in total magnitude and relative contribution of the different cloud types (Fig. 6a). This is because SW atmospheric absorption is small and most of the SW extinction is due to scattering.

As SW atmospheric absorption is small, the surface and TOA CREs are of a similar magnitude, and the in-atmosphere CRE is small. The small in-atmosphere CRE that does occur (Fig. 6c) is due to a combination of increased atmospheric path length for radiation reflected by low cloud and absorption of near-infrared radiation by cloud. With an in-cloud CRE of approximately
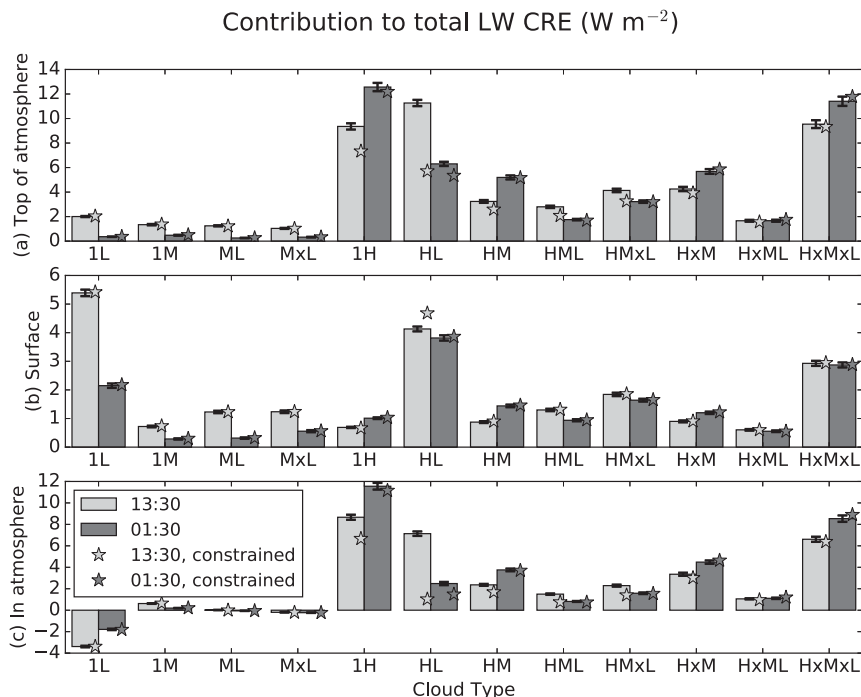
FIG. 7. As in Fig. 6, but for LW CRE.

$5\,\mathrm{W\,m^{-2}}$, HxMxL, HL, and 1L once again have the largest CREs.

Compared to the SW CRE, the LW CRE shows more complex behavior. For the TOA (Fig. 7a), since the LW CCRE largely depends on the cloud-top temperature (as shown in Fig. 5b), the standout cloud types become HxMxL, HL, and 1H. In contrast to the SW TOA CRE isolated low cloud (1L) has a rather small impact on the LW CRE at the TOA, as it has a small CCRE (Fig. 5b). The three dominant cloud types account for approximately 60% of the regional mean LW CRE at the TOA so, as with the SW CRE, other cloud types make a nonnegligible contribution to the regional mean CRE.

At the surface, the LW CCRE is strongly dependent on cloud-base height. Consequently, the contributions of the different cloud types to the regional mean LW CRE are quite different from those for the LW CRE at the TOA. The three dominant cloud types for the LW CRE at the surface are 1L, HL, and HxMxL. Coincidentally, these match the three dominant cloud types in the SW CRE. As for the SW CRE at all heights, and the LW CRE at the TOA, other cloud types make nonnegligible contributions to the regional mean LW CRE at the surface.

As the TOA and surface LW CREs are quite different, the in-atmosphere CREs show a large range between cloud types. In the presence of isolated low clouds, the net LW irradiance increases at the surface

and decreases at the TOA. Since the magnitude of the former is greater than the latter, isolated low clouds cause LW radiative cooling of the atmosphere, as shown in Fig. 7c. For high-top clouds, the decrease in CRE at the TOA is larger in magnitude than the increase in CRE at the surface, so high cloud causes LW radiative heating of the atmosphere. Adding low cloud beneath high cloud leads to a larger magnitude LW irradiance increase at the surface, so that the LW radiative heating of the atmosphere is less than it would be in the absence of the low clouds (e.g., during the day, HL occurs more frequently than 1H and has a larger CRE at the TOA but a smaller effect on the in-atmosphere CRE). Midlevel-top clouds lead to cooling above the cloud and heating beneath the cloud; this affects the vertical temperature gradient of the atmosphere but has little effect on the vertically integrated atmospheric heating.

At the TOA and surface, the difference between calculations for day and night are generally less than $5\,\mathrm{W\,m^{-2}}$, and of varying sign depending on cloud type (larger surface LW CRE in the day for 1L but smaller TOA LW CRE in the day for 1H). These day–night differences are primarily due to the contrasting frequencies of occurrence between day and night (Fig. 4), except for the HL cloud type, where the day–night differences are primarily due to differences in the CCRE (Fig. 5).

Uncertainty in LW contributions to the CRE is estimated from the constrained dataset (star symbols in
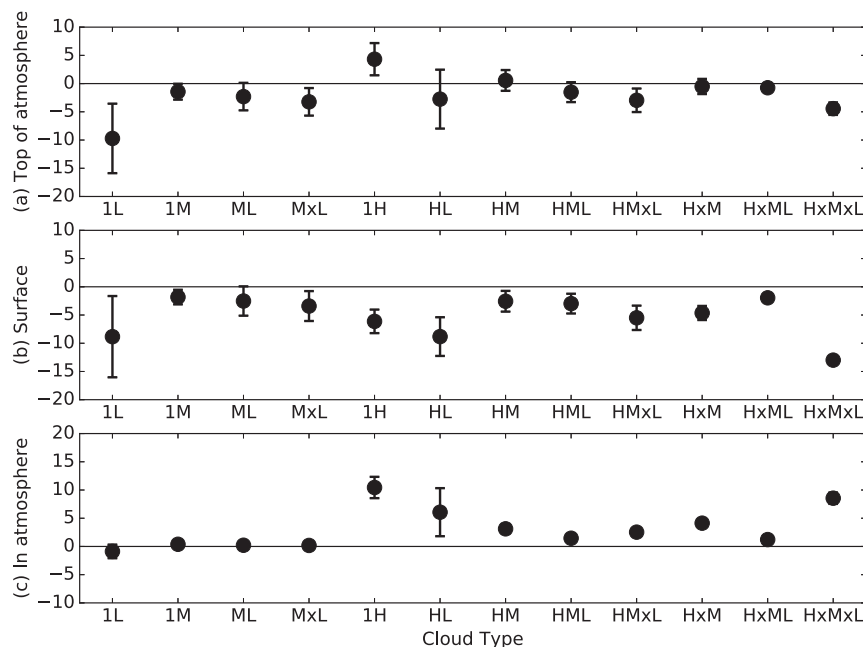
FIG. 8. Contribution to the diurnal mean total (i.e., SW + LW) CRE from each cloud type for June–September 2006–10 over SWA, based on SOCRATES calculations. Error bars show the combined uncertainty resulting from the diurnal mean approximation, the constrained calculation (which exclude CCCM group profiles where the SOCRATES–CERES TOA differences are large, as explained in section 2e), and the limited sampling. These uncertainties are calculated separately for the SW and LW and are combined in quadrature.

Figs. 5–7). The low-cloud misattribution hypothesis posits that the CCCM dataset overestimates extinction by high cloud because of missing low cloud. However, we have no objective estimate of how this missing low cloud will affect the frequencies of the different cloud types. Consequently, we use the original cloud type frequencies to calculate CRE contributions in the constrained dataset; only the mean CCRE is changed. As a result, TOA differences between the full and constrained datasets follow the pattern described for the mean CCRE. At the surface the differences are much smaller. However, the constrained dataset results in a larger contribution from HL during the day to the surface LW CRE. This results in a difference of $6 \, \mathrm{W \, m^{-2}}$ between the two calculations for flux into the atmosphere.

Figure 8 shows the approximate diurnal mean total (i.e., SW + LW) cloud radiative effects. This is the sum of the SW and LW diurnal mean approximations. The error bars show the combined uncertainty resulting from the SW and LW diurnal mean approximations, differences between the full and refined datasets, and sampling errors. These three sources of uncertainty are estimated separately for the SW and LW radiation, resulting in a total of six values that are combined by summing in quadrature.

The diurnal mean total irradiances tend to be small because of cancellation between LW and SW CREs. For some cloud types, uncertainty is quite large (up to $\pm 7 \, \mathrm{W \, m^{-2}}$) at the TOA and surface, but the uncertainty is generally much smaller for fluxes into the atmosphere. At the TOA, the 1L cloud type has the largest magnitude net CRE, as the decrease in net downwelling SW TOA irradiance resulting from low clouds is much larger than the increase in net downwelling LW TOA irradiance. Most other cloud types also have a negative effect on the TOA net downwelling irradiance, although for many cloud types this is not certain. Isolated high cloud (1H) is the only cloud type that definitely leads to an increase in the net TOA irradiance. All cloud types reduce the net downwelling irradiance at the surface, because of the reduction in SW radiation reaching the surface being larger than the increase in downwelling LW radiation. 1L leads to a small reduction in the flux into the atmosphere, but all other cloud types increase the flux into the atmosphere.

4. Sensitivity of radiative fluxes to low-cloud cover errors

As noted in the introduction and our analysis of the CCCM cloud types, low cloud is common in SWA. Yet
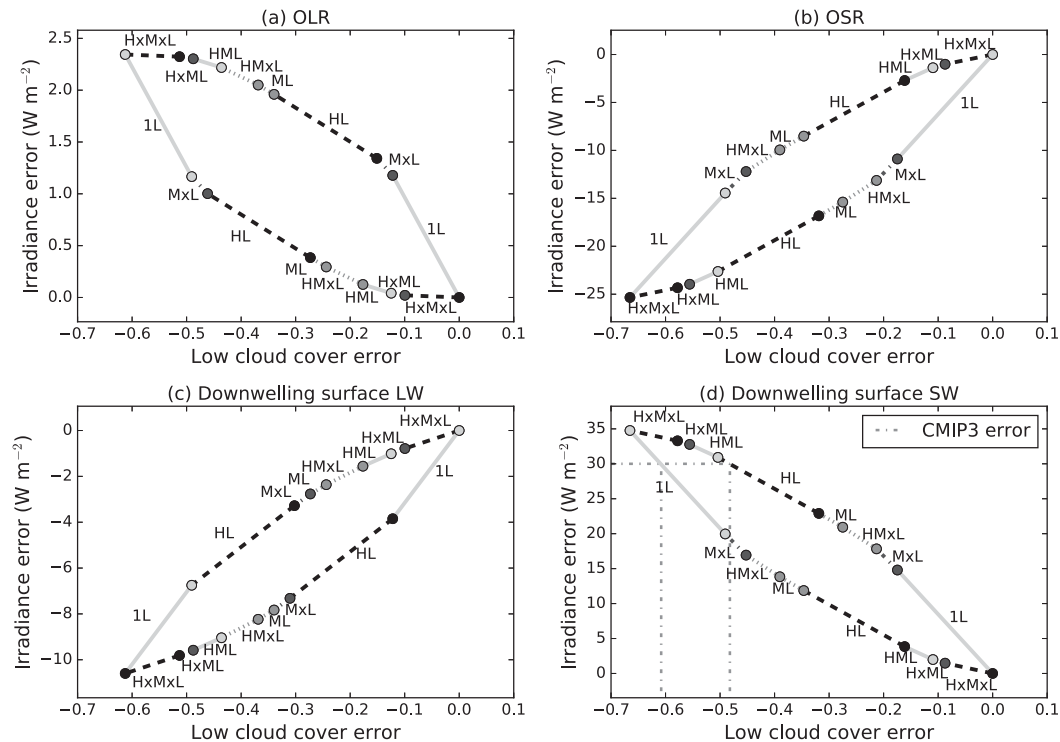
FIG. 9. Cumulative change in diurnal mean irradiance as a result of removing low cloud for different cloud types for June–September 2006–10. Calculated as the difference between the original calculations and further calculations where all cloud water content beneath 680 hPa is removed. Each labeled line shows the change in low-cloud cover (horizontal extent of the line) and irradiance (vertical extent of the line) caused by removing low cloud for the cloud type indicated on the label. The cloud types are plotted according to the magnitude of the change in irradiance per unit change in cloud cover. Both increasing and decreasing order are plotted, which show the lower and upper bounds for the irradiance change for a given change in low-cloud cover, respectively. The gray dash-dotted lines show the range of low-cloud cover errors required to produce the modeled irradiance bias of 30 W m^{-2} identified by Knippertz et al. (2011). The low-cloud cover increments (x axis) for each cloud type match the frequency of occurrence shown in Fig. 4 As we show changes in diurnal mean irradiance, the SW values are based on cloud cover at 1330 LT and the LW values are based on the average of the 0130 and 1330 LT low-cloud cover.

low-cloud cover is generally underestimated in climate models, which is thought to be responsible for large surface SW radiation biases in these models (e.g., Knippertz et al. 2011; Hannak et al. 2017). In this section we assess the potential role of low-altitude cloud cover errors in contributing to radiation budget biases through sensitivity studies. To this end, we estimate irradiance sensitivity to low-cloud cover errors by comparing the existing SOCRATES calculations with further calculations that mimic the low-cloud bias in models by removing cloud water content beneath 680 hPa. The bias resulting from removing all low clouds, which we denote $\Delta CRE_{-\text{low}}$, is calculated by subtracting the CRE based on the original calculations from the CRE based on the new calculations where low cloud is removed. Like the CRE, this can be separated into contributions from the different cloud types $\Delta CRE^k_{-\text{low}}$.

Figure 9 shows the cumulative change in approximate diurnal mean irradiances from $\Delta CRE^k_{-\text{low}}$ for all cloud types that include low cloud. Note that for ease of comparison to the Hannak et al. (2017) study, we show downwelling surface irradiances rather than net (down minus up) downwelling surface irradiance as in all other figures. First, $\Delta CRE^k_{-\text{low}}$ shows large variation between cloud types. The irradiances are most sensitive to changes in low-cloud cover for 1L, while the irradiances are least sensitive to changes in low-cloud cover for HxMxL. This is because $\Delta CRE^k_{-\text{low}}$ strongly depends on the presence of other cloud in the profile. For example, for the 1L cloud type, removing the low cloud results in clear sky, so much more SW radiation reaches the surface. On the contrary, for HxMxL, removing the low cloud has a much smaller impact on the downwelling surface SW radiation, as the remaining cloud above 680 hPa reflects a large amount of SW radiation (Fig. 9d).

So that Fig. 9 can be used to estimate the likely irradiance error for a given low-cloud cover error, the changes in both low-cloud cover and irradiances associated with each cloud type are plotted cumulatively. Clearly, as $\Delta\text{CRE}^k_{-\text{low}}$ depends on cloud type, there is a range of possible irradiances for a given low-cloud cover error. To capture this, we plot the cumulative irradiance errors in order of both increasing and decreasing magnitude of $\Delta\text{CRE}^k_{-\text{low}}$ per unit change in low-cloud cover, which correspond to the minimum and maximum irradiance error for a given change in low-cloud cover respectively. The relative importance of low cloud to different cloud types is similar for both SW and LW irradiances at both TOA and the surface. However, the relative importance of low cloud to HL compared to other cloud types for the downwelling surface LW irradiance is larger than for the SW and surface LW irradiances, because of high cloud having little effect on the downwelling LW irradiance at the surface.

The net (SW + LW) error resulting from low-cloud cover errors may be as large as $24\,\text{W}\,\text{m}^{-2}$ for the downwelling surface irradiance and $23\,\text{W}\,\text{m}^{-2}$ for the outgoing irradiance at the TOA. Errors of this magnitude in an atmospheric model are likely to impact on the regional circulation and precipitation. For example, Li et al. (2015) linked radiative perturbations of a similar magnitude to monthly mean precipitation changes of up to $60\,\text{mm}\,\text{month}^{-1}$ in simulations of the WAM.

Coming back to the issue with large surface SW radiation biases found in models, Knippertz et al. (2011) showed a multimodel mean bias of approximately $30\,\text{W}\,\text{m}^{-2}$ in downwelling surface SW irradiances over SWA during June–September using simulations from phase 3 of the Coupled Model Intercomparison Project (CMIP3). A similar analysis of simulations from the Year of Tropical Convection (YOTC) revealed a multimodel mean bias of about $25\,\text{W}\,\text{m}^{-2}$. Based on Fig. 9d, the CMIP3 bias is equivalent to a low-cloud cover error of between -0.48 and -0.61, as illustrated by the thin broken gray lines. Similarly, the YOTC bias (not shown) is equivalent to a low-cloud cover error of between -0.37 and -0.55. Since such large low-cloud cover biases are required to produce the SW irradiance biases seen in models, we conclude that models must also underestimate the occurrence of other cloud types in this region.

In summary, low-cloud cover errors are expected to lead to large errors in diurnal mean SW irradiances, up to $35\,\text{W}\,\text{m}^{-2}$ for the downwelling surface irradiance and up to $25\,\text{W}\,\text{m}^{-2}$ for the OSR. These are offset somewhat by smaller changes in LW irradiances of up to $11\,\text{W}\,\text{m}^{-2}$ at the surface and $2\,\text{W}\,\text{m}^{-2}$ at the TOA. Errors of this magnitude are sufficient to affect the WAM circulation in atmospheric models. However, the $30\,\text{W}\,\text{m}^{-2}$ mean bias in the downwelling surface SW irradiance simulated by CMIP3 climate models is unlikely to be solely as a result of low cloud errors.

5. Summary

Southern West Africa (SWA) is a region where clouds are poorly understood, and the large-scale circulation is sensitive to radiative perturbations. To better understand cloud–radiation interactions in this region, we have classified clouds into 12 distinct types based on vertical structure and quantified the radiative effect of these cloud types at the surface, TOA, and on heating and cooling of the atmosphere. We have focused in particular on low clouds, which are poorly understood since they are often obscured in satellite imagery and there is currently a lack of surface observations in the region.

SWA experiences many different cloud types; no single cloud type dominates in terms of either frequency of occurrence or radiative effect. The most frequent cloud types are 1L, 1H, HL, and HxMxL (see Fig. 3 for definitions), which have frequencies of 12%, 14%, 19%, and 10%, respectively. Contributions from different cloud types to the regional mean cloud radiative effect depend not only on their frequencies, but also on their mean coincident cloud radiative effects (CCREs), which are linked to cloud thickness in the SW and cloud-top and cloud-base height in the LW.

The regional energy budget links cloud radiative effects to precipitation and circulation (e.g., Hill et al. 2016). As a summary of the contribution of different cloud types to the regional diurnal mean energy budget, Fig. 10 shows how the net effect on atmospheric heating for each cloud type can be explained by contrasting SW and LW radiation effects at the surface and TOA. Uncertainty is denoted by the plus and minus values, rounded to the nearest integer, and shows the combined uncertainty resulting from uncertainty in the diurnal mean approximation, differences between the full and refined datasets, and sampling errors. To reduce the number of panels, we show the four most frequent cloud types independently and divide the remaining cloud types into two categories, midlevel top and high top. All cloud types lead to a net cooling of the surface, ranging from approximately $2\,\text{W}\,\text{m}^{-2}$ for ML to $13\,\text{W}\,\text{m}^{-2}$ for HxMxL. 1H results in an increase in the net downwelling irradiance at the TOA ($4\,\text{W}\,\text{m}^{-2}$), but all other cloud types have the opposite effect. The 1L type leads to small cloud radiative cooling of the atmosphere, but all other cloud types lead to heating.

Uncertainty in the cloud radiative effects remains a result of the limited diurnal sampling and differences
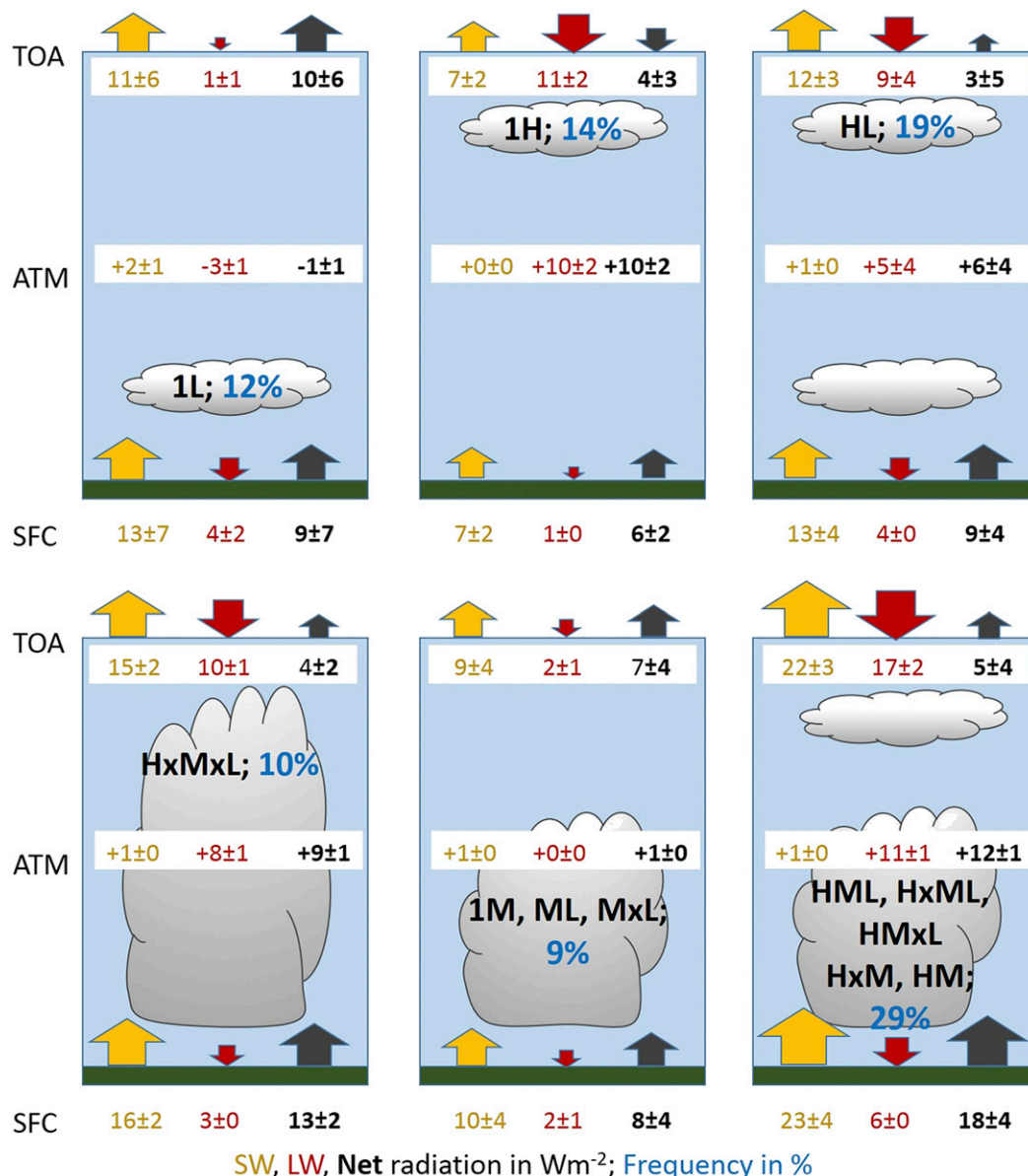
FIG. 10. Schematic illustrating the contribution of different cloud types to the diurnal mean radiation budget of the atmosphere of SWA for June–September 2006–10. The direction each arrows point in indicates the direction of the CRE for that cloud type and the area of each arrow is proportional to the magnitude of the CRE. The plus and minus values indicate uncertainty, as explained in the text. To reduce the number of panels in the schematic, we show the four most frequent cloud types (1L, 1H, HL, and HxMxL) and the remaining cloud types are split into midlevel top and high top and the combined radiative effects are shown. Note that all values are rounded to the nearest integer.

between the calculations and CERES measurements. The frequency of low clouds may also be underestimated in the CCCM data product. Our calculations have been evaluated by comparison of the TOA irradiances with coincident CERES measurements. We find good agreement for SW and nighttime LW irradiances, but our calculations underestimate the OLR during the daytime. This is thought to be due to problems identifying low cloud from satellites, which may lead to the misattribution of low-cloud extinction to higher clouds in the CCCM dataset.

Focusing on low cloud, we have shown that it occurs much more frequently below other clouds (30%) than by itself (12%). As a result, passive satellites, which are unable to detect low cloud beneath other clouds, will miss much of the low cloud in SWA. Isolated low cloud

(1L) is the only cloud type that contributes a net cooling to the atmosphere. This is due to LW radiative cooling of the atmosphere, which predominantly occurs within the cloud, and is due to an increase in the downwelling LW irradiance. This is offset by relatively large (compared to the other cloud types) SW radiative heating of the atmosphere, because of gaseous absorption of the increased upwelling SW radiation that is reflected by the cloud.

Discontiguous low cloud plays a less obvious role in reducing cloud radiative heating of the atmosphere. When low cloud co-occurs with higher cloud, the radiative heating of the atmosphere resulting from the higher cloud tends to be larger than the cooling effect of the low cloud. However, the radiative heating of the atmosphere is less than it would be in the absence of the low cloud. For example, Fig. 10 shows that cloud radiative heating of the atmosphere is less for HL than for 1H, even though HL occurs more often (19% compared to 14%). Further calculations where low cloud is removed as described in the previous section show that the presence of low cloud in HL reduces the cloud radiative heating of the atmosphere by $2 \, \text{W m}^{-2}$. The presence of low cloud also reduces the cloud radiative heating of the atmosphere for the other cloud types where discontiguous low cloud is present (i.e., ML, HML, and HxML, in addition to HL). The total cloud radiative heating of the atmosphere is $37 \, \text{W m}^{-2}$, with the cooling from low cloud being approximately $-4 \, \text{W m}^{-2}$.

Sensitivity to underestimating low-cloud cover was examined by comparing calculations with and without low cloud; underestimating low-cloud cover led to a downwelling SW irradiance error of up to $33 \, \text{W m}^{-2}$ and an OSR error of up to $24 \, \text{W m}^{-2}$. Thus, low cloud errors are unlikely to be solely responsible for the $25–30 \, \text{W m}^{-2}$ multimodel mean surface downwelling SW errors in SWA identified in climate models (Knippertz et al. 2011; Hannak et al. 2017). However, the effect of underestimating low cloud is undoubtedly significant. Errors of a similar magnitude have been linked to large changes in monsoon circulation and monsoon precipitation in regional climate simulations (Li et al. 2015).

We anticipate that these calculations will provide a useful tool for evaluating cloud–radiation interactions in this region in atmospheric models, and the method can be extended to other regions, or even globally. This will require model diagnostics that assign cloud types to model columns in the same manner as this study. Many climate models already include the Cloud Feedback Model Intercomparison Project (CFMIP) Observation Simulator Package (COSP; Bodas-Salcedo et al. 2011),

which could be used to diagnose the frequency of different cloud profiles within the model and thereby generate the diagnostics required. Such diagnostics would provide a useful tool for evaluating the cloud in models. We see two key advantages to this method for evaluating models. First, separating different cloud types will help to reveal compensating errors between different cloud types; similarly, separating frequency of occurrence and CCRE for each cloud type will reveal compensating error for individual cloud types, such as the ''too few, too bright'' problem in climate models (Nam and Quaas 2012). Second, as the formation and dissipation of different cloud types are linked to different physical processes, attributing model errors to different cloud types will aid identification of problematic cloud processes in the model.

Cloud and radiation measurements taken during the DACCIWA field campaign (Flamant et al. 2017) provide a complementary dataset to the calculations described here, with better identification of low cloud and diurnal sampling, but with a limited time period (June–July 2016) and worse spatial sampling. The DACCIWA project is also working with weather services in SWA to extend the availability of existing surface measurements and provide further cloud data. Future work will exploit these surface-based datasets alongside satellite observations to refine our understanding of low cloud and its influence on the regional energy budget.

REFERENCES

Adler, B., N. Kalthoff, and L. Gantner, 2017: Nocturnal low-level clouds over southern West Africa analysed using high-resolution simulations. *Atmos. Chem. Phys.*, **17**, 899–910, https://doi.org/10.5194/acp-17-899-2017.

Baran, A. J., P. Field, K. Furtado, J. Manners, and A. Smith, 2013: A new high- and low-frequency scattering parameterization for cirrus and its impact on a high-resolution numerical weather prediction model. *AIP Conf. Proc.*, **1531**, 716–719, https://doi.org/10.1063/1.4804870.

——, P. Hill, D. Walters, S. C. Hardiman, K. Furtado, P. R. Field, and J. Manners, 2016: The impact of two coupled cirrus microphysics–radiation parameterizations on the temperature and specific humidity biases in the tropical tropopause layer in a climate model. *J. Climate*, **29**, 5299–5316, https://doi.org/10.1175/JCLI-D-15-0821.1.

Birch, C. E., J. H. Marsham, D. J. Parker, and C. M. Taylor, 2014: The scale dependence and structure of convergence fields preceding the initiation of deep convection. *Geophys. Res. Lett.*, **41**, 4769–4776, https://doi.org/10.1002/2014GL060493.

Bodas-Salcedo, A., and Coauthors, 2011: COSP: Satellite simulation software for model assessment. *Bull. Amer. Meteor. Soc.*, **92**, 1023–1043, https://doi.org/10.1175/2011BAMS2856.1.

——, P. G. Hill, K. Furtado, K. D. Williams, P. R. Field, J. C. Manners, P. Hyder, and S. Kato, 2016: Large contribution of supercooled liquid clouds to the solar radiation budget of the Southern Ocean. *J. Climate*, **29**, 4213–4228, https://doi.org/10.1175/JCLI-D-15-0564.1.

Bouniol, D., F. Couvreux, P.-H. Kamsu-Tamo, M. Leplay, F. Guichard, F. Favot, and E. J. O'Connor, 2012: Diurnal and seasonal cycles of cloud occurrences, types, and radiative impact over West Africa. *J. Appl. Meteor. Climatol.*, **51**, 534–553, https://doi.org/10.1175/JAMC-D-11-051.1.

Collow, A. B., V. P. Ghate, M. A. Miller, and L. C. Trabachino, 2016: A one-year study of the diurnal cycle of meteorology, clouds and radiation in the West African Sahel region. *Quart. J. Roy. Meteor. Soc.*, **142**, 16–29, https://doi.org/10.1002/qj.2623.

Cook, K. H., and E. K. Vizy, 2006: Coupled model simulations of the West African monsoon system: Twentieth- and twenty-first-century simulations. *J. Climate*, **19**, 3681–3703, https://doi.org/10.1175/JCLI3814.1.

Cusack, S., A. Slingo, J. M. Edwards, and M. Wild, 1998: The radiative impact of a simple aerosol climatology on the Hadley Centre atmospheric GCM. *Quart. J. Roy. Meteor. Soc.*, **124**, 2517–2526, https://doi.org/10.1002/qj.49712455117.

Dewitte, S., L. Gonzalez, N. Clerbaux, A. Ipe, C. Bertrand, and B. D. Paepe, 2008: The Geostationary Earth Radiation Budget edition 1 data processing algorithms. *Adv. Space Res.*, **41**, 1906–1913, https://doi.org/10.1016/j.asr.2007.07.042.

Edwards, J. M., and A. Slingo, 1996: Studies with a flexible new radiation code. I: Choosing a configuration for a large-scale model. *Quart. J. Roy. Meteor. Soc.*, **122**, 689–719, https://doi.org/10.1002/qj.49712253107.

Flamant, C., and Coauthors, 2018: The Dynamics–Aerosol–Chemistry–Cloud Interactions in West Africa field campaign: Overview and research highlights. *Bull. Amer. Meteor. Soc.*, **99**, 83–104, https://doi.org/10.1175/BAMS-D-16-0256.1.

Futyan, J. M., J. E. Russel, and J. E. Harries, 2005: Determining cloud forcing by cloud type from geostationary satellite data. *Geophys. Res. Lett.*, **32**, L08807, https://doi.org/10.1029/2004GL022275.

Ham, S.-H., and Coauthors, 2017: Cloud occurrences and cloud radiative effects (CREs) from CERES-*CALIPSO-CloudSat*-MODIS (CCCM) and *CloudSat* radar-lidar (RL) products. *J. Geophys. Res. Atmos.*, **122**, 8852–8884, https://doi.org/10.1002/2017JD026725.

Hannak, L., P. Knippertz, A. H. Fink, A. Kniffka, and G. Pante, 2017: Why do global climate models struggle to represent low-level clouds in the West African summer monsoon? *J. Climate*, **30**, 1665–1687, https://doi.org/10.1175/JCLI-D-16-0451.1.

Harries, J. E., and Coauthors, 2005: The Geostationary Earth Radiation Budget Project. *Bull. Amer. Meteor. Soc.*, **86**, 945–960, https://doi.org/10.1175/BAMS-86-7-945.

Hartmann, D. L., M. E. Ockert-Bell, and M. L. Michelsen, 1992: The effect of cloud type on Earth's energy balance: Global analysis. *J. Climate*, **5**, 1281–1304, https://doi.org/10.1175/1520-0442(1992)005<1281:TEOCTO>2.0.CO;2.

Hill, P. G., R. P. Allan, J. C. Chiu, and T. H. M. Stein, 2016: A multi-satellite climatology of clouds, radiation and precipitation in southern West Africa and comparison to climate models. *J. Geophys. Res. Atmos.*, **121**, 10 857–10 879, https://doi.org/10.1002/2016JD025246.

Hong, Y., G. Liu, and J.-L. F. Li, 2016: Assessing the radiative effects of global ice clouds based on *CloudSat* and *CALIPSO* measurements. *J. Climate*, **29**, 7651–7674, https://doi.org/10.1175/JCLI-D-15-0799.1.

Hourdin, F., and Coauthors, 2010: AMMA-Model Intercomparison Project. *Bull. Amer. Meteor. Soc.*, **91**, 95–104, https://doi.org/10.1175/2009BAMS2791.1.

Kato, S., 2003: Computation of domain-averaged shortwave irradiance by a one-dimensional algorithm incorporating correlations between optical thickness and direct incident radiation. *J. Atmos. Sci.*, **60**, 182–193, https://doi.org/10.1175/1520-0469(2003)060<0182:CODASI>2.0.CO;2.

——, S. Sun-Mack, W. F. Miller, F. G. Rose, Y. Chen, P. Minnis, and B. A. Wielicki, 2010: Relationships among cloud occurrence frequency, overlap and effective thickness derived from *CALIPSO* and *CloudSat* merged vertical profiles. *J. Geophys. Res.*, **115**, D00H28, https://doi.org/10.1029/2009JD012277.

——, and Coauthors, 2011: Improvements of top-of-atmosphere and surface irradiance computations with *CALIPSO*-, *CloudSat*-, and MODIS-derived cloud and aerosol properties. *J. Geophys. Res.*, **116**, D19209, https://doi.org/10.1029/2011JD016050.

Knippertz, P., A. H. Fink, R. Schuster, J. Trentmann, J. M. Schrage, and C. Yorke, 2011: Ultra-low clouds over the southern West African monsoon region. *Geophys. Res. Lett.*, **38**, L21808, https://doi.org/10.1029/2011GL049278.

——, M. J. Evans, P. R. Field, A. H. Fink, C. Liousse, and J. H. Marsham, 2015a: The possible role of local air pollution in climate change in West Africa. *Nat. Climate Change*, **5**, 815–822, https://doi.org/10.1038/nclimate2727.

——, and Coauthors, 2015b: The DACCIWA Project: Dynamics–Aerosol–Chemistry–Cloud Interactions in West Africa. *Bull. Amer. Meteor. Soc.*, **96**, 1451–1460, https://doi.org/10.1175/BAMS-D-14-00108.1.

Li, R., J. Jin, S.-Y. Wang, and R. R. Gillies, 2015: Significant impacts of radiation physics in the Weather Research and Forecasting model on the precipitation and dynamics of the West African monsoon. *Climate Dyn.*, **44**, 1583–1594, https://doi.org/10.1007/s00382-014-2294-2.

Loeb, N., 2008: CERES Level 2 NEWS CCCM Aqua-FM3-MODIS-CAL-CS HDF File—Release B1. NASA Langley Atmospheric Science Data Center DAAC, https://doi.org/10.5067/aqua/ceres/news_cccm-fm3-modis-cal-cs_l2.relb1.

Mace, G. G., Q. Zhang, M. Vaughan, R. Marchand, G. Stephens, C. Trepte, and D. Winker, 2009: A description of hydrometeor layer occurrence statistics derived from the first year of merged *CloudSat* and *CALIPSO* data. *J. Geophys. Res.*, **114**, D00A26, https://doi.org/10.1029/2007JD009755.

Marsham, J. H., N. S. Dixon, L. Garcia-Carreras, G. M. S. Lister, D. J. Parker, P. Knippertz, and C. E. Birch, 2013: The role of moist convection in the West African monsoon system:

Insights from continental-scale convection-permitting simulations. *Geophys. Res. Lett.*, **40**, 1843–1849, https://doi.org/10.1002/grl.50347.

Miller, M. A., V. P. Ghate, and R. K. Zahn, 2012: The radiation budget of the West African Sahel and its controls: A perspective from observations and global climate models. *J. Climate*, **25**, 5976–5996, https://doi.org/10.1175/JCLI-D-11-00072.1.

Minnis, P., and Coauthors, 2011: CERES Edition-2 cloud property retrievals using TRMM VIRS and *Terra* and *Aqua* MODIS data—Part I: Algorithms. *IEEE Trans. Geosci. Remote Sens.*, **49**, 4374–4400, https://doi.org/10.1109/TGRS.2011.2144601.

Nam, C. C. W., and J. Quaas, 2012: Evaluation of clouds and precipitation in the ECHAM5 general circulation model using *CALIPSO* and *CloudSat* satellite data. *J. Climate*, **25**, 4975–4992, https://doi.org/10.1175/JCLI-D-11-00347.1.

——, S. Bony, J.-L. Dufresne, and H. Chepfer, 2012: The 'too few, too bright' tropical low-cloud problem in CMIP5 models. *Geophys. Res. Lett.*, **39**, L21801, https://doi.org/10.1029/2012GL053421.

Nicholson, S. E., and J. P. Grist, 2003: The seasonal evolution of the atmospheric circulation over West Africa and equatorial Africa. *J. Climate*, **16**, 1013–1030, https://doi.org/10.1175/1520-0442(2003)016<1013:TSEOTA>2.0.CO;2.

Oreopoulos, L., N. Cho, and D. Lee, 2017: New insights about cloud vertical structure from *CloudSat* and *CALIPSO* observations. *J. Geophys. Res. Atmos.*, **122**, 9280–9300, https://doi.org/10.1002/2017JD026629.

Paeth, H., and Coauthors, 2011: Progress in regional downscaling of West African precipitation. *Atmos. Sci. Lett.*, **12**, 75–82, https://doi.org/10.1002/asl.306.

Rodwell, M. J., and T. Jung, 2008: Understanding the local and global impacts of model physics changes: An aerosol example. *Quart. J. Roy. Meteor. Soc.*, **134**, 1479–1497, https://doi.org/10.1002/qj.298.

Roehrig, R., D. Bouniol, F. Guichard, F. Hourdin, and J.-L. Redelsperger, 2013: The present and future of the West African monsoon: A process-oriented assessment of CMIP5 simulations along the AMMA transect. *J. Climate*, **26**, 6471–6505, https://doi.org/10.1175/JCLI-D-12-00505.1.

Schrage, J. M., S. Augustyn, and A. H. Fink, 2007: Nocturnal stratiform cloudiness during the West African monsoon. *Meteor. Atmos. Phys.*, **95**, 73–86, https://doi.org/10.1007/s00703-006-0194-7.

Schuster, R., A. H. Fink, and P. Knippertz, 2013: Formation and maintenance of nocturnal low-level stratus over the southern West African monsoon region during AMMA 2006. *J. Atmos. Sci.*, **70**, 2337–2355, https://doi.org/10.1175/JAS-D-12-0241.1.

Stein, T. H. M., D. J. Parker, J. Delanoë, N. S. Dixon, R. J. Hogan, P. Knippertz, R. I. Maidment, and J. H. Marsham, 2011: The vertical cloud structure of the West African monsoon: A 4 year climatology using *CloudSat* and *CALIPSO*. *J. Geophys. Res.*, **116**, D22205, https://doi.org/10.1029/2011JD016029.

——, ——, R. J. Hogan, C. E. Birch, C. E. Holloway, G. M. S. Lister, J. H. Marsham, and S. J. Woolnough, 2015: The representation of the West African monsoon vertical cloud structure in the Met Office Unified Model: An evaluation with *CloudSat*. *Quart. J. Roy. Meteor. Soc.*, **141**, 3312–3324, https://doi.org/10.1002/qj.2614.

Taylor, J. P., J. M. Edwards, M. D. Glew, P. Hignett, and A. Slingo, 1996: Studies with a flexible new radiation code. II: Comparisons with aircraft short-wave observations. *Quart. J. Roy. Meteor. Soc.*, **122**, 839–861, https://doi.org/10.1002/qj.49712253204.

Tompkins, A. M., 2005: Influence of aerosol climatology on forecasts of the African easterly jet. *Geophys. Res. Lett.*, **32**, L10801, https://doi.org/10.1029/2004GL022189.

Tselioudis, G., W. Rossow, Y. Zhang, and D. Konsta, 2013: Global weather states and their properties from passive and active satellite cloud retrievals. *J. Climate*, **26**, 7734–7746, https://doi.org/10.1175/JCLI-D-13-00024.1.

van der Linden, R., A. H. Fink, and R. Redl, 2015: Satellite-based climatology of low-level continental clouds in southern West Africa during the summer monsoon season. *J. Geophys. Res. Atmos.*, **120**, 1186–1201, https://doi.org/10.1002/2014JD022614.

Wang, J., W. B. Rossow, and Y. Zhang, 2000: Cloud vertical structure and its variations from a 20-yr global rawinsonde dataset. *J. Climate*, **13**, 3041–3056, https://doi.org/10.1175/1520-0442(2000)013<3041:CVSAIV>2.0.CO;2.